INTERNATIONAL JOURNAL OF ENERGY RESEARCH
Int. J. Energy Res. 2011; **35:**1325–1339
Published online 2 June 2011 in Wiley Online Library (wileyonlinelibrary.com). DOI: 10.1002/er.1873

Effects of catalyst layer structure and wettability on liquid water transport in polymer electrolyte membrane fuel cell

Prodip K. Das[1,‡], Xianguo Li[1,*,†], Zhong Xie[2] and Zhong-Sheng Liu[2]

[1]Department of Mechanical and Mechatronics Engineering, University of Waterloo, 200 University Avenue West, Waterloo, ON N2L 3G1, Canada
[2]NRC Institute for Fuel Cell Innovation, 4250 Wesbrook Mall, Vancouver, BC V6T 1W5, Canada

SUMMARY

Optimal water levels in polymer electrolyte membrane (PEM) fuel cells are the key to prevent liquid water flooding and to reduce membrane dry out. A good understanding of liquid water transport is therefore essential to maintain an optimum water balance. In this study, a two-dimensional, two-phase, volume-averaged numerical model is developed and used to simulate the effect of catalyst layer structure and its surface wettability on liquid water transport in the cathode catalyst layer (CCL) of PEM fuel cells. The model is capable of handling liquid water transport across both the catalyst and gas diffusion layers. The simulation results are compared with literature, and a good agreement is found. The highest liquid water saturation in the CCL is observed under the rib, and the lowest value is observed under the flow channel. It is also observed that the wetting and geometric characteristics of CCL have significant influence on the liquid water transport, and the mobile liquid water saturation in a hydrophilic catalyst layer decreases with CCL surface wettability, that is, lower CCL contact angle yields lower liquid water saturation. Copyright © 2011 John Wiley & Sons, Ltd.

KEY WORDS

catalyst layer; two-phase flow; liquid water transport; surface wettability; numerical simulation; PEM fuel cell

Correspondence

*Xianguo Li, Department of Mechanical and Mechatronics Engineering, University of Waterloo, 200 University Avenue West, Waterloo, ON N2L 3G1, Canada.
[†]E-mail: xianguo.li@uwaterloo.ca
[‡]Present address: Lawrence Berkeley National Laboratory, 1 Cyclotron Road, Berkeley, CA 94720, USA. E-mail: pkdas@lbl.gov

Received 2 December 2010; Revised 22 March 2011; Accepted 28 April 2011

1. INTRODUCTION

Fuel cells are promising energy conversion devices, which directly extract electricity from the chemical energy of fuels without polluting the environment [1–4]. In particular, polymer electrolyte membrane (PEM) fuel cell is considered one of the most promising alternatives for automotive applications. Although PEM fuel cell has drawn immense attention over the last decades as a high-efficiency and low-emission power source, a number of technical barriers are suppressing it from being competitive for automotive applications. Specifically, the activation loss, expensive catalyst, and liquid water flooding are hindering the commercialization of PEM fuel cell. These factors are directly coupled with transport phenomena in micron-sized constituents, such as cathode catalyst layer (CCL), gas diffusion layer (GDL), and electrolyte membrane, in a PEM fuel cell. Given the small scales, it is extremely difficult to investigate transport phenomena in a PEM fuel cell experimentally, both intrusively and nonintrusively. Therefore, mathematical and numerical models become the only means to provide meaningful insights on the physical and electrochemical phenomena occurring in a PEM fuel cell. Conversely, it is impossible to optimize and design an improved cell without a good understanding of transport phenomena. Because several phases co-exist within the micron-sized porous constituents of a PEM fuel cell, careful attention is always required for developing an accurate mathematical model with all the known physical and electrochemical phenomena that are happening during the operation of a PEM fuel cell. In particular, liquid water conservation equations have been erroneously represented ignoring the fact that two-phase flow in porous media significantly differs from single-phase flow [5–8].

Water management in PEM fuel cells is a crucial issue, which determines the cell performance [9–16]. This issue is important because too little water will cause membrane

dehydration and too much water can flood the fuel cell, causing less reactant to reach the active catalyst sites and consequently decreasing the cell performance. Hence, a proper water management is critical to achieve the full potential of a PEM fuel cell. Furthermore, liquid water is one of the key factors responsible for the degradation of electrolyte membrane. Because Springer *et al.* [9] and Bernardi and Verbrugge [10] developed a one-dimensional PEM fuel cell model including various modes of water transport, numerous research works have been focused on the analysis of water transport and management [11–30]. Most of them addressed liquid water transport in the electrolyte membrane and GDL. None of them specifically addressed liquid water transport inside the CCL. Furthermore, these studies were based on the assumption that the production of liquid water is at the CCL/GDL interface or the catalyst layer is very thin, whereas the highest reaction rate occurs at the membrane/CCL interface [31], and the CCL thickness should be higher than 10 μm to obtain an optimum performance from a PEM fuel cell [32]. Therefore, the approximation of thin CCL and considering the CCL as an interface seem to be insufficient to explore the overall liquid water transport in CCL. Although liquid water flooding in CCL likely occurs before that in the gas flow channel (GFC) and GDL because water is produced at the CCL from the electrochemical reaction and is expelled from the CCL to the GFC through the GDL, the studies related to the CCL flooding are elusive.

In this study, our goal is to investigate liquid water transport in PEM fuel cell catalyst layer. *In situ* measurement inside a catalyst layer is very difficult. Even if possible, for instance using nuclear magnetic resonance microscopy [33] or neutron radiography [34], it can only yield a qualitative visualization of liquid water distribution. Therefore, liquid water transport in CCL is investigated solving the fundamental transport equations numerically. Because liquid water transport involves several transport and physical processes, the widely used M^2 model is insufficient for this purpose [35]. Furthermore, the M^2 model considers liquid and gas phases a homogeneous mixture, and it has a narrow applicability, limited to the situations of flow without change of phase and flow without phase production due to other physical processes [36]. Here, a multifluid volume-averaged mathematical model for transport phenomena is used [37], and the effects of CCL structure and surface wettability on the liquid water transport and cell performance are investigated using a parametric study.

2. MODEL FORMULATION

2.1. Physical problem

In PEM fuel cells, humidified H_2 gas is supplied under pressure into the anode gas flow channel, which diffuses through the GDL until it reaches the anode catalyst layer, and dissociates into protons and electrons via electro-oxidation reaction at the catalyst surface. The protons are transported through the membrane to the CCL, whereas the electrons are transported via the external circuit to the cathode side that provides electrical energy into the external circuit. Conversely, humidified air is supplied to the cathode gas flow channel, where O_2 diffuses through the GDL until it reaches the CCL and forms water reacting with protons and electrons. The overall electrochemical reaction occurring in a PEM fuel cell can be represented by the following reaction:

$$2H_2+O_2\rightarrow 2H_2O + \text{Heat} + \text{Electric Energy} \qquad (1)$$

A schematic of a PEM fuel cell is shown Figure 1 as well as the computational domain (right) under consideration. Although the main focus is given to the CCL, the computational domain includes GDL, bipolar plate (BP), and GFC. Because of the symmetry along the cell height, only half of the flow channel and rib are considered, where the dashed line in the right part of Figure 1 indicates the line of symmetry.

2.2. Governing equations

The gas phase transport in PEM fuel cell cathode is described by the microscopic conservation equations of mass, momentum, and species [1,2]. Using a volume-averaged technique, we summarized the conservation equations of mass, momentum, and species in gas phase for the present model as follows [37–40]:

$$\nabla\cdot\left(\varepsilon_g\left\langle\rho_g\right\rangle^g\langle u_g\rangle^g\right)=\Gamma_{M,g} \qquad (2)$$

$$\nabla\cdot\left(\varepsilon_g\left\langle\rho_g\right\rangle^g\langle u_g\rangle^g\langle u_g\rangle^g\right)+\nabla\left(\varepsilon_g\langle P_g\rangle^g\right)-\langle P_g\rangle^g\nabla\left(\varepsilon_g\right) -\nabla\cdot\left(\varepsilon_g\langle\tau_g\rangle^g\right)=\Gamma_{F,g} \qquad (3)$$

$$\nabla\cdot\left(\varepsilon_g\left\langle\rho_g\right\rangle^g\left\langle w_g^\alpha\right\rangle^g\langle u_g\rangle^g+\varepsilon_g\left\langle J_g^\alpha\right\rangle^g\right)=\Gamma_{S,g}^\alpha \qquad (4)$$

where the subscript g represents the gas phase and the triangular bracket with superscript g represents the phase-averaged value. Here, ε is the volume fraction, ρ is the density, u is the velocity, P is the pressure, τ is the viscous stress tensor, w^α is the mass fraction of species α, J^α is the mass flux of species α, and Γ is the source term.

The liquid phase in PEM fuel cell cathode consists of liquid water only. Therefore, the volume-averaged conservation of mass and momentum equations are derived as follows [37]:

$$\nabla\cdot\left(\varepsilon_l\langle\rho_l\rangle^l\langle u_l\rangle^l\right)=\Gamma_{M,l} \qquad (5)$$

$$\nabla\cdot\left(\varepsilon_l\langle\rho_l\rangle^l\langle u_l\rangle^l\langle u_l\rangle^l\right)+\nabla\left(\varepsilon_l\langle P_l\rangle^l\right)-\langle P_l\rangle^l\nabla(\varepsilon_l) -\nabla\cdot\left(\varepsilon_l\langle\tau_l\rangle^l\right)=\Gamma_{F,l} \qquad (6)$$

where the subscript l represents the liquid phase and the triangular bracket with superscript l represents the phase-averaged value. If we neglect the viscous effect and

Int. J. Energy Res. 2011; **35**:1325–1339 © 2011 John Wiley & Sons, Ltd.
DOI: 10.1002/er

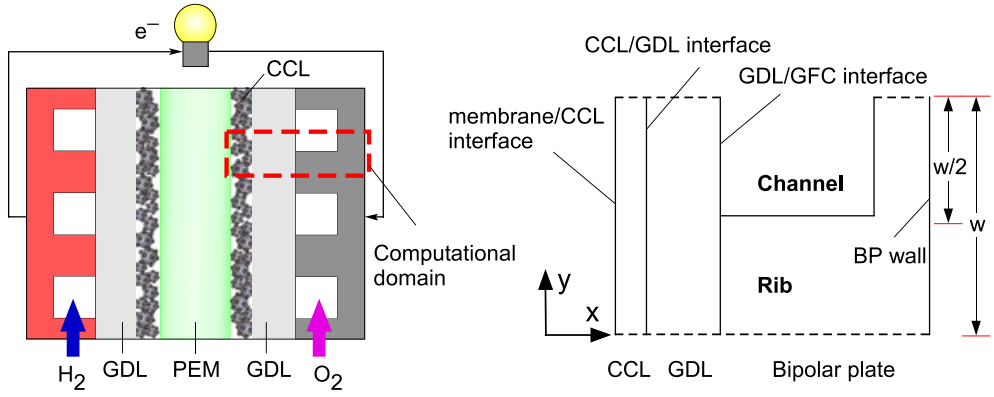

Figure 1. Schematic of a PEM fuel cell with computational domain (left), indicated by the dashed rectangle, and a detailed depiction of the computational domain (right).

combine Eqns 5 and 6 with the aid of Eqns 2 and 3, the liquid water equation can be written as follows [37]:

$$\nabla\cdot\left(\frac{Kk_{r,l}}{\mu_l}\langle\rho_l\rangle\frac{dP_c}{ds_l}\nabla s_l+\frac{k_{r,l}\mu_g}{k_{r,g}\mu_l}\langle\rho_l\rangle\langle u_g\rangle^g\right)=\Gamma_{M,l} \quad (7)$$

where K is the permeability, k_r is the relative permeability, s_l is the liquid water saturation, μ is the viscosity, and $\langle\rho_l\rangle$ is the volume-averaged liquid phase density. The capillary pressure, P_c, is the difference between the gas phase and liquid phase pressures, which is modeled by the following empirical correlation [1,17,28,41]:

$$P_c=\gamma\cos\theta_c\left(\frac{\varepsilon}{K}\right)^{0.5}F(s_l) \quad (8)$$

where γ is the surface tension between the gas phase and liquid phase, θ_c is the contact angle, and $F(s_l)$ is the Leverett function.

For the electron and proton transports, the solid phase and membrane phase potential equations are written as follows:

$$\nabla\cdot\left(\varepsilon_s\sigma_s^{eff}\nabla\langle\Phi_s\rangle^s\right)=-4FA_vR_{c,red} \quad (9)$$

$$\nabla\cdot\left(\varepsilon_m\sigma_m^{eff}\nabla\langle\Phi_m\rangle^m\right)=4FA_vR_{c,red} \quad (10)$$

where the subscripts s and m represent the solid phase and membrane phase, respectively. Here, σ^{eff} is the effective conductivity, Φ is the potential, and F is the Faraday constant. The effective conductivities are estimated using the expressions available in literature [42], whereas the rate of reaction, $R_{c,red}$, is estimated using the Butler–Volmer equation as follows:

$$R_{c,red}=\frac{J_0^{O_2}}{4F}\left(\frac{c_{O_2}}{c_{O_2,ref}}\right)\left\{\exp\left(\frac{\alpha_a nF\eta_c}{RT}\right)-\exp\left(-\frac{\alpha_c nF\eta_c}{RT}\right)\right\} \quad (11)$$

where $J_0^{O_2}$ is the reference current density at the reference oxygen concentration of $c_{O_2,ref}$, c_{O_2} is the oxygen concentration, and α_a and α_c are the apparent transfer coefficients for the anodic and cathodic reactions, respectively. The term n represents the number of electrons transferred in the electrochemical reaction, and η_c represents the activation overpotential, which is the driving force for the electrochemical reaction. The catalyst reactive surface area per unit volume, A_v, is a function of catalyst mass loading per unit area of cathode (m_{Pt}), catalyst surface area per unit mass of the catalyst (A_s), and catalyst layer thickness (δ_{CL}) that is estimated as follows [37]:

$$A_v=\frac{A_s m_{Pt}}{\delta_{CL}} \quad (12)$$

2.3. Boundary conditions and source terms

To solve the volume-averaged governing equations numerically, the following boundary conditions are applied. The species concentrations are defined as follows:

$$c_{O_2}=\frac{0.21(P-R_HP_{sat})}{RT} \quad \text{for } \partial\Omega\in \text{GDL/GFC interface} \quad (13)$$

$$c_{H_2O}=\frac{R_HP_{sat}}{RT} \quad \text{for } \partial\Omega\in \text{GDL/GFC interface} \quad (14)$$

where P and T are the operating pressure and temperature, respectively, R_H is the relative humidity, R is the gas constant, and $\partial\Omega$ is the computational boundary. For the gas phase conservation of momentum equation, the gas pressure at the GDL/GFC interface is defined equal to the operating pressure because the momentum equation is simplified in the porous GDL and CCL as the Darcy's law. In all other boundaries, an insulation or symmetry boundary condition is applied.

The boundary condition for liquid water equation at the membrane/CCL interface is quite complex because liquid water can diffuse through the membrane or the electro-osmotic drag can bring more liquid water to the CCL. Thus, a simplified boundary condition is applied at the membrane/CCL interface for the liquid water equation, where it is

assumed that the net water transport by the back-diffusion and electro-osmotic drag is zero. Conversely, liquid saturation at the GDL/GFC interface is defined as follows:

$$s_{\mathrm{l}} = s_{\mathrm{l,GFC}} \quad \text{for } \partial\Omega \in \text{GDL/GFC interface} \qquad (15)$$

where $s_{\mathrm{l,GFC}}$ is a known liquid saturation at the GDL/GFC interface that is considered to be zero or a small value (usually in the order 10^{-3} or lower) for numerical stability.

The von Neumann boundary condition is applied to all the boundaries for the solid phase potential equation, except the BP wall. The boundary conditions for the solid phase potential can be summarized as follows:

$$\Phi_{\mathrm{s}} = V_{\mathrm{cell}} \quad \text{for } \partial\Omega \in \text{BP wall} \qquad (16)$$

$$\nabla\Phi_{\mathrm{s}} = 0 \quad \text{for } \partial\Omega \notin \text{BP wall} \qquad (17)$$

The von Neumann boundary condition is also used for the membrane phase potential equation for all the boundaries. Hence, the boundary conditions for the membrane phase potential are summarized as follows:

$$-\sigma_{\mathrm{m}}^{\mathrm{eff}} \nabla\Phi_{\mathrm{m}} = J_{\mathrm{m}} \quad \text{for } \partial\Omega \in \text{membrane/CCL interface} \qquad (18)$$

$$\nabla\Phi_{\mathrm{m}} = 0 \quad \text{for } \partial\Omega \notin \text{membrane/CCL interface} \qquad (19)$$

where J_{m} is the membrane phase current density that is the total current density at the membrane/CCL interface. The source terms for the volume-averaged conservation equations (Eqns 2–6) in the GDL and CCL are listed in Table I. It is worthwhile to note that the detailed derivations of the volume-averaged conservation equations and the source terms are available in Ref. [37].

3. NUMERICAL TECHNIQUE AND IMPLEMENTATION

3.1. Solution procedure

The governing equations containing mass, momentum, species, and charges are solved using COMSOL Multiphysics® (COMSOL, Inc., 1 New England Executive Park, Suite 350, Burlington, MA 01803, USA), using a FEM to solve the system of coupled PDEs. The computational domain is initially discretized into a triangular mesh, and the Lagrangian elements of second order (quadratic elements) are used. The UMFPACK solver is chosen to solve the governing PDEs because it is faster than other solvers available in COMSOL Multiphysics®. However, the UMFPACK solver requires higher computer memory compared with the other solvers. Hence, the SPOOLES solver is also used in some cases, particularly for the refined meshes, because it can save half of the memory. The detailed solution procedure is also available in Ref. [37].

3.2. Grid independent solution

To ensure that the numerical results are grid independent, we estimated the governing variables in different grid sizes. Figure 2 shows the variations of liquid water saturation along the dimensionless distance from the membrane/CCL interface to the GDL/GFC interface for three different grid sizes. Here, the line represents the result of a coarser grid, and the symbols are for the finer grids as indicated in the legend, namely, grid 1 (45 409 triangular elements), grid 2 (60 046 triangular elements),

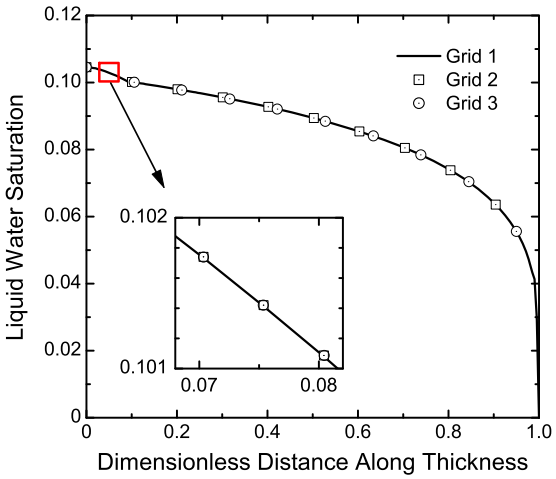

Figure 2. Liquid water saturation profiles along the dimensionless thickness of CCL and GDL for different grids at $y = 3w/4$.

Table I. Source terms for the volume-averaged conservation equations in GDL and CCL.

Source term	GDL	CCL
$\Gamma_{\mathrm{M,g}}$	$A\left(P_{\mathrm{sat}} - x_{\mathrm{g}}^{\mathrm{H_2O}} \langle P_{\mathrm{g}} \rangle^{\mathrm{g}}\right)$	$-M_{\mathrm{O_2}} A_{\mathrm{v}} R_{\mathrm{c,red}} + A\left(P_{\mathrm{sat}} - x_{\mathrm{g}}^{\mathrm{H_2O}} \langle P_{\mathrm{g}} \rangle^{\mathrm{g}}\right)$
$\Gamma_{\mathrm{F,g}}$	$-\frac{\varepsilon_{\mathrm{g}}\mu_{\mathrm{g}}}{K k_{\mathrm{r,g}}} \langle u_{\mathrm{g}} \rangle^{\mathrm{g}}$	$-\frac{\varepsilon_{\mathrm{g}}\mu_{\mathrm{g}}}{K k_{\mathrm{r,g}}} \langle u_{\mathrm{g}} \rangle^{\mathrm{g}}$
$\Gamma_{\mathrm{S,g}}^{\mathrm{H_2O}}$	$A\left(P_{\mathrm{sat}} - x_{\mathrm{g}}^{\mathrm{H_2O}} \langle P_{\mathrm{g}} \rangle^{\mathrm{g}}\right)$	$A\left(P_{\mathrm{sat}} - x_{\mathrm{g}}^{\mathrm{H_2O}} \langle P_{\mathrm{g}} \rangle^{\mathrm{g}}\right)$
$\Gamma_{\mathrm{S,g}}^{\mathrm{O_2}}$	0	$-M_{\mathrm{O_2}} A_{\mathrm{v}} R_{\mathrm{c,red}}$
$\Gamma_{\mathrm{M,l}}$	$-A\left(P_{\mathrm{sat}} - x_{\mathrm{g}}^{\mathrm{H_2O}} \langle P_{\mathrm{g}} \rangle^{\mathrm{g}}\right)$	$2M_{\mathrm{H_2O}} A_{\mathrm{v}} R_{\mathrm{c,red}} - A\left(P_{\mathrm{sat}} - x_{\mathrm{g}}^{\mathrm{H_2O}} \langle P_{\mathrm{g}} \rangle^{\mathrm{g}}\right)$
$\Gamma_{\mathrm{F,l}}$	$-\frac{\varepsilon_{\mathrm{l}}\mu_{\mathrm{l}}}{K k_{\mathrm{r,l}}} \langle u_{\mathrm{l}} \rangle^{\mathrm{l}}$	$-\frac{\varepsilon_{\mathrm{l}}\mu_{\mathrm{l}}}{K k_{\mathrm{r,l}}} \langle u_{\mathrm{l}} \rangle^{\mathrm{l}}$

and grid 3 (104 837 triangular elements). The results are plotted across the CCL and GDL thicknesses under the flow channel at $y = 3w/4$. Because all the grids show almost identical liquid saturation results, the numerical results in the following sections are presented for a grid size of 60 000 triangular elements or higher.

4. RESULTS AND DISCUSSIONS

In this section, the results of two-dimensional numerical simulations are presented. The grid independency test does not always ensure an accurate estimation if the governing equations are implemented improperly. Therefore, a numerical validation is an essential part of a numerical simulation. In the following sections, the numerical simulation results are first validated, and then the results of a parametric study are presented.

4.1. Numerical validation

The most popular approach to validate numerical simulation results for a PEM fuel cell is to compare a polarization curve with experimental data. Here, a half cell approach is considered to model the CCL; hence, it is required to estimate ohmic and concentration overpotentials and mixed potential for accurately generating a polarization curve. Furthermore, the experimental results reported in various PEM fuel cells literature also lack information on several physical and electrochemical parameters. In some cases, replicating the published results is found to be very difficult because of the missing information or parameter values. Hence, the comparison with an experimental polarization curve does not always ensure numerical validity unless all the physical and electrochemical parameters involved in the experiment are known.

In this study, we use a different approach to validate numerical simulation results than the typical polarization curve approach. Here, numerical results are compared with analytical model data that are available in literature [43]. It is worthwhile to note that the analytical data of activation overpotential have already been compared with experimental data [32], and the same analytical model is used to generate the liquid water saturation data [43]. Figure 3 depicts the comparison of numerical results with analytical model results for two different current densities as indicated in the legends. The liquid water saturations are plotted across the CCL thickness at two different locations, namely, $y = w/2$ and $y = w$, from the line of symmetry as shown in Figure 1. The lines represent the analytical model results of liquid saturation across the CCL thickness, and the symbols represent the numerical simulation results for a CCL having a contact angle of 80°. All the parameters used in the numerical simulation are the same as the base case, except the GDL properties. The values of GDL thickness, porosity, and contact angle are considered as 300 μm, 0.5, and 100°, respectively, whereas the base case parameters are listed in Table II.

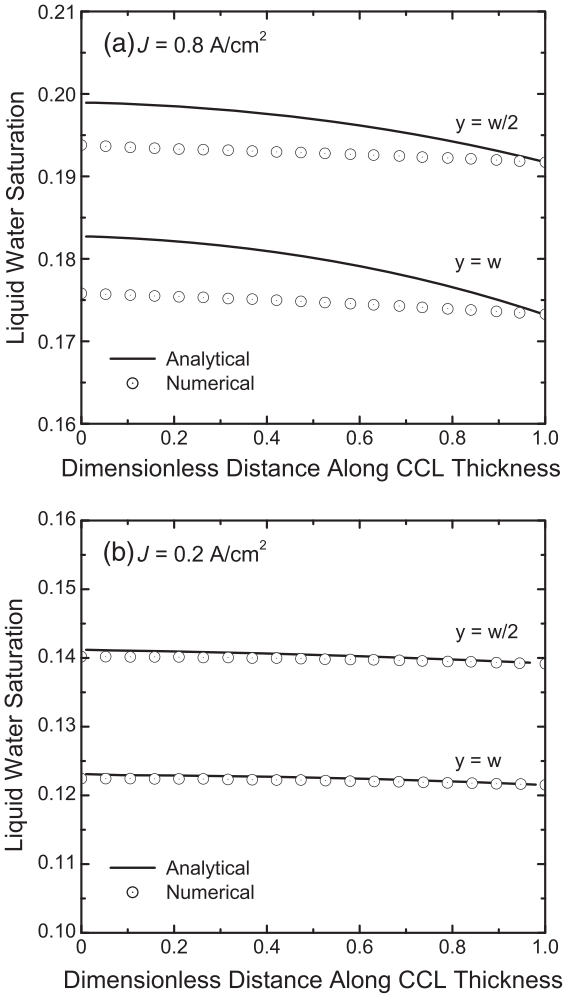

Figure 3. Validation of numerical results with the analytical model data. The lines represent the liquid saturation across the CCL estimated using an analytical model [43], whereas the symbols represent the numerical results at two different locations under the flow channel as indicated in the legends.

Table II. Parameters used in the numerical simulation for the base case.

Parameter	Value
Channel width (mm)	1
Channel height (mm)	1
Operating temperature (°C)	80
Operating pressure (atm)	3
Operating current density (A/cm^2)	0.8
Relative humidity (%)	100
GDL thickness (μm)	200
GDL contact angle (°C)	110
GDL porosity	0.6
CCL thickness (μm)	20
Catalyst loading per unit area (mg/cm^2)	0.3
%wt of platinum in CCL	0.2
%wt of Nafion in CCL	0.3

For a high current density ($J = 0.8$ A/cm^2), the analytical model shows higher liquid saturation than the numerical results. This discrepancy is mainly due to the assumption made in the analytical model, and one of the assumptions was constant oxygen concentration across the CCL thickness. In reality, the oxygen concentration varies significantly across the CCL thickness at high current density, and it will be lower at the membrane/CCL interface than the oxygen concentration at the CCL/GDL interface. Because the reaction rate is also a function of oxygen concentration, an assumption of higher oxygen concentration at the membrane/CCL interface implies a higher reaction rate; hence, liquid water production from the electrochemical reaction is also higher. Therefore, the analytical expression of liquid water saturation at the CCL of a PEM fuel cell overestimates liquid water saturation at high current density. At the same time, we should point out that the difference between the numerical results and analytical data at the high current density is about 3% to 4% at the membrane/CCL interface, and this difference reduces as we move toward the CCL/GDL interface.

At low current density ($J = 0.2$ A/cm^2), the variation of oxygen concentration in the CCL is relatively low. Hence, the assumption used in the analytical solution of liquid water profile in the CCL makes the analytical expression valid for the low current densities. Because of this, Figure 3b shows almost identical liquid saturation profiles for both the numerical simulation and analytical estimation. Although a small variation between the numerical and analytical results is still visible near the membrane/CCL interface, it can be again attributed to the assumption of uniform oxygen concentration used in the analytical model. It is worthwhile to emphasize that no specific and detailed measurements of liquid water saturation in CCL of PEM fuel cells are available in open literature that can be used to further validate the present model. The attempt we made in this study to compare the numerical simulation results with the analytical model data is perhaps the only approach available in open literature other than the typical polarization curve approach. Therefore, it is reasonable to claim that the numerical simulation results are accurate with respect to the analytical model data because it matches the limiting case (low current density), and the comparison shown in Figure 3b can serve as the validation of numerical results presented here.

4.2. Effect of catalyst layer porosity

The catalyst layer is considered as a macro-homogenous layer; therefore, the physical structure of CCL can be quantified by its porosity. Obviously, the pores inside a CCL are random, and it is not possible to physically quantify a random structure. Hence, it is assumed that the catalyst layer's porosity is sufficient to describe the physical nature of a macro-homogenous catalyst layer. The catalyst layer porosity depends on the platinum (Pt) and Nafion loadings; hence, the results are presented as the functions of Pt and Nafion loadings.

Figure 4 shows the variations of liquid water saturation and oxygen mass fraction with different Nafion loadings (weight percentage of Nafion) along the through-plane direction of CCL and GDL at $y = w/4$. The parameter values used in these calculations are listed in Table II. For low Nafion loading ($\%N \leq 30\%$), the variations of liquid water saturation are negligible for the entire thickness of CCL and GDL. For a high Nafion loading ($\%N > 30\%$), Nafion loading increases liquid water saturation inside the catalyst layer. For the entire range of Nafion loadings shown in Figure 4, the liquid saturation remains almost identical throughout the GDL thickness. Because the Nafion loading is inversely proportional to CCL porosity, it seems that the CCL porosity does not have any significant effect on the liquid water saturation inside the GDL. When oxygen concentrations for the various Nafion loadings are compared, we see a variation in the oxygen mass fraction (shown in Figure 4b). The oxygen mass

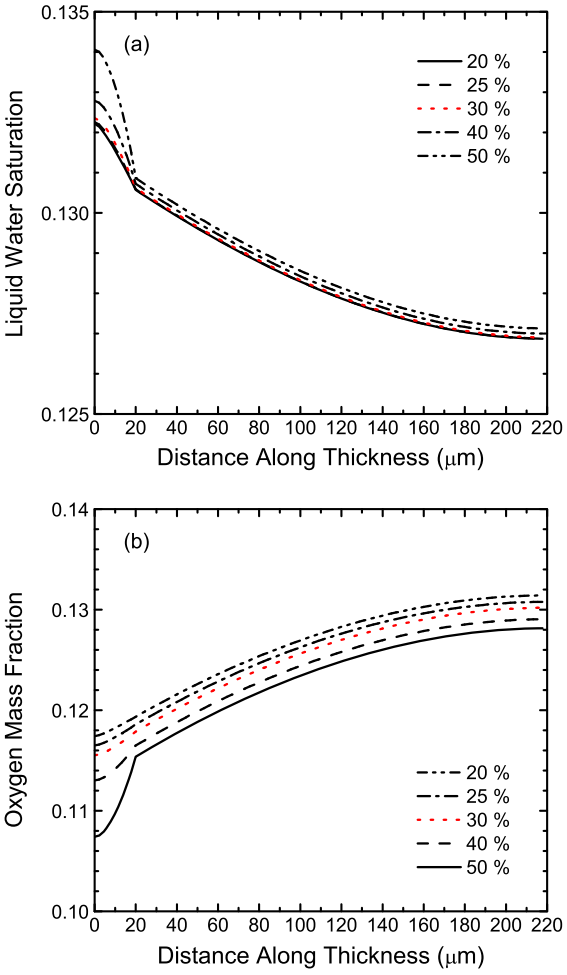

Figure 4. Variations of liquid water saturation and oxygen mass fraction with Nafion loadings along the through-plane direction of CCL and GDL under the rib at $y = w/4$ for a current density of 0.8 A/cm^2.

Int. J. Energy Res. 2011; **35**:1325–1339 © 2011 John Wiley & Sons, Ltd.
DOI: 10.1002/er

fraction variation is about 10% between the highest and lowest Nafion loadings at the membrane/CCL interface. Because the effective oxygen diffusivity decreases with the catalyst layer porosity, the effective oxygen diffusivity will be lower at higher Nafion loadings. Hence, the oxygen transport is hindered by the Nafion loadings. Conversely, the production of liquid water inside the catalyst layer is significantly dictated by the electrochemical reaction, hence by the activation overpotential.

The local activation overpotential profiles along the CCL thickness for different Nafion loadings are shown in Figure 5. Clearly, the local activation overpotential decreases with Nafion loading at the membrane/CCL interface. Because local activation overpotential is highest at the membrane/CCL interface, the value at the membrane/CCL interface will correspond to the cell's activation loss. Hence, the value at the membrane/CCL interface is simply referred as 'activation overpotential', and the value along the CCL thickness is referred as 'local activation overpotential'. For the high Nafion loading, the effective protonic conductivity for the catalyst layer increases significantly, which provides lower membrane phase potential inside the catalyst layer, and hence, it reduces the activation overpotential and the electrochemical reaction rate. Therefore, the production of liquid water is low for high Nafion loading. Hence, the variation of liquid water saturation profile observed in Figure 4a is the net increase of liquid water saturation due to the porosity reduction and the activation overpotential reduction. At the same time, the results shown in Figure 4 also indicate that the optimum performance of a PEM fuel cell should be obtained when a Nafion loading of about 30% is considered for the CCL.

Figure 6 shows the variations of liquid water saturation and oxygen mass fraction along the through-plane direction of CCL and GDL for five different Pt loadings

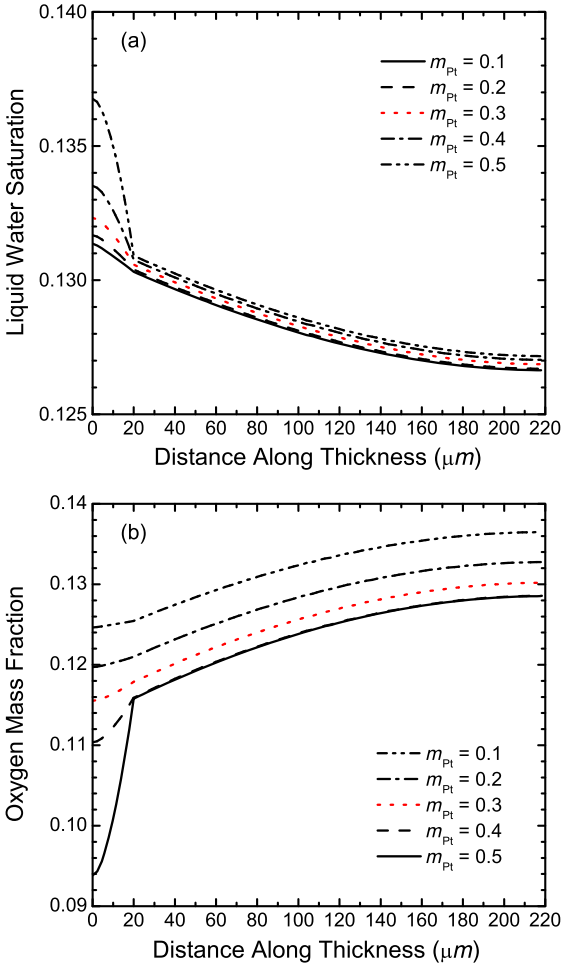

Figure 6. Variations of liquid water saturation and oxygen mass fraction with Pt loadings along the through-plane direction of CCL and GDL at $y = w/4$.

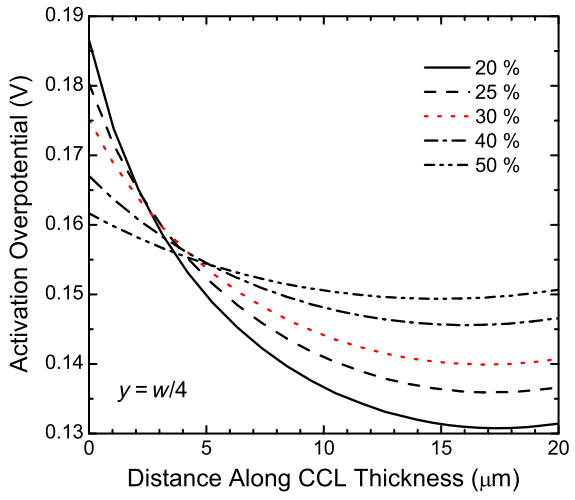

Figure 5. Local activation overpotential profiles along the catalyst layer thickness at $y = w/4$ for different Nafion loadings.

(mg/cm^2) as indicated in the legend. The parameter values used in these calculations are listed in Table II. For low Pt loading ($m_{Pt} \leq 0.3$ mg/cm^2), the variations of liquid water saturation with Pt loadings are almost negligible for the entire GDL thickness. This behavior is almost identical to the various Nafion loading result shown in Figure 4. For high Pt loading ($m_{Pt} > 0.3$ mg/cm^2), Pt loading increases liquid water saturation significantly inside the CCL, but the variation of liquid saturation is relatively small inside the GDL. This is because the Pt loading changes the CCL porosity, and the CCL porosity does not have any significant effect on liquid water saturation inside the GDL. Unlike Figure 4, the oxygen mass fractions with various Pt loadings show a significant variation throughout the CCL and GDL thicknesses. The variation is even more prominent inside the catalyst layer. Comparing Figure 6 with Figure 4, we observe about 30% reduction in the oxygen mass fraction when Pt loading changes from a value of 0.1 to 0.5 mg/cm^2. It is worthwhile to mention that Figure 4 is plotted as a function of %wt of Nafion

membrane, whereas Figure 5 shows the result as a function of Pt loading in mg/cm^2. Therefore, the highest value of Pt loading corresponds to a different porosity than the porosity for the highest value of Nafion loading. Nonetheless, Figure 6 depicts that the optimum Pt loading should be in the range of 0.3 mg/cm^2 or lower, which is within the range of our earlier prediction [32].

The local activation overpotential profiles along the CCL thickness with five different Pt loadings are shown in Figure 7. The activation overpotential decreases significantly with Pt loading that is mainly due to the better electrochemical reaction at the membrane/CCL interface. Although the higher Pt loading reduces catalyst layer porosity and hinders oxygen transport, it provides a better transport of electrons and protons. It should be mentioned that these results are calculated by changing Pt loadings only. Both the %wt of platinum and %wt of Nafion membrane are kept constant. Therefore, the higher Pt loading also represents a higher Nafion volume fraction, which provides a higher effective protonic conductivity for the membrane phase inside the CCL. Although a 26% reduction in the activation overpotential is possible to achieve by increasing Pt loading from a value of 0.1 to 0.5 mg/cm^2, it might not be favorable for the PEM fuel cells because of the cost of platinum. Therefore, an optimum Pt loading is always desirable.

4.3. Effect of catalyst layer contact angle

Figure 8 shows the variations of liquid water saturation with different CCL contact angles at various locations of CCL and GDL along the through-plane and in-plane directions for a current density of 0.8 A/cm^2. Here, Figure 8a shows liquid water saturation profiles under the flow channel ($y = 3w/4$), and Figure 8b shows liquid water saturation profiles under the rib ($y = w/4$). Conversely, Figure 8c shows the results along the in-plane direction

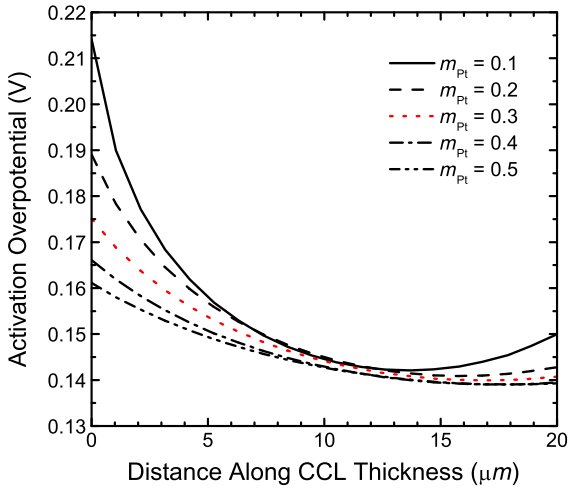

Figure 7. Local activation overpotential profiles along the catalyst layer thickness at $y = w/4$ for different Pt loadings.

inside the CCL at two different locations. The lines in Figure 8c represent the results near the membrane/CCL interface at $x = 1$ μm, and the symbols represent the results near the CCL/GDL interface at $x = 19$ μm. The last part of Figure 8 shows the variations of liquid water saturation along the in-plane direction at the middle of the GDL. The parameter values used to estimate the results shown in Figure 8 are listed in Table II, except the CCL contact angles that are indicted in the figure legends.

Clearly, the contact angles for hydrophilic CCL do not have any significant effect on liquid water saturation in the GDL under the flow channel ($y = 3w/4$). For the CCL, the contact angles show a change in the liquid saturation values. The higher the contact angles, the higher the liquid saturations. The variation in liquid saturation profile is small compared with the variation observed in our previous study that was based on the one-dimensional analytical expressions of liquid water saturation for the CCL [43]. However, the trends of saturation profiles remain identical. As mentioned earlier, the analytical expressions of liquid water saturation in the CCL always overestimate liquid saturation at high current density. The variations observed between the numerical results and the results of Ref. [43] can be attributed to the assumptions used in the analytical formulation and the current density value used in the numerical simulation ($J = 0.8$ A/cm^2). Conversely, liquid saturation profile under the rib ($y = w/4$) shows almost identical trend in both CCL and GDL for low contact angles. For high contact angles, the variations are more prominent inside the CCL. Because the catalyst layer needs to be well hydrated for better electrochemical reaction and oxygen transport is hindered by liquid water, it seems a hydrophilic catalyst layer with lower contact angles ($\theta_c \leq 70^\circ$) would perform better because it can provide a smoother transition for liquid water transport at the CCL/GDL interface.

For in-plane direction inside the CCL, liquid water saturation profiles are shown in Figure 8c. Here, the lines show the results near the membrane/CCL interface, and the symbols show the results near the CCL/GDL interface. For both cases, the contact angles do not show any significant effect on the liquid water saturation for $\theta_c \leq 70^\circ$. For high contact angle ($\theta_c > 80^\circ$), a high liquid water saturation near the membrane/CCL interface than the CCL/GDL interface is observed. In fact, the capillary pressure is less for the higher contact angle. Hence, the driving force is less, which eventually reduces the liquid water transport. Because liquid saturation profiles inside the CCL remain almost unchanged for $\theta_c \leq 70^\circ$, it can be concluded again that a CCL with lower contact would perform better for both the electrochemical reaction and oxygen transport. Like the through-plane direction under the flow channel, the liquid saturation profiles remain independent of the CCL contact angles in the in-plane direction inside the GDL as illustrated in Figure 8d. However, a small variation between the liquid water saturation profiles is observed under the rib. Because the CCL contact angles have strong influence on liquid water

Int. J. Energy Res. 2011; **35**:1325–1339 © 2011 John Wiley & Sons, Ltd.
DOI: 10.1002/er

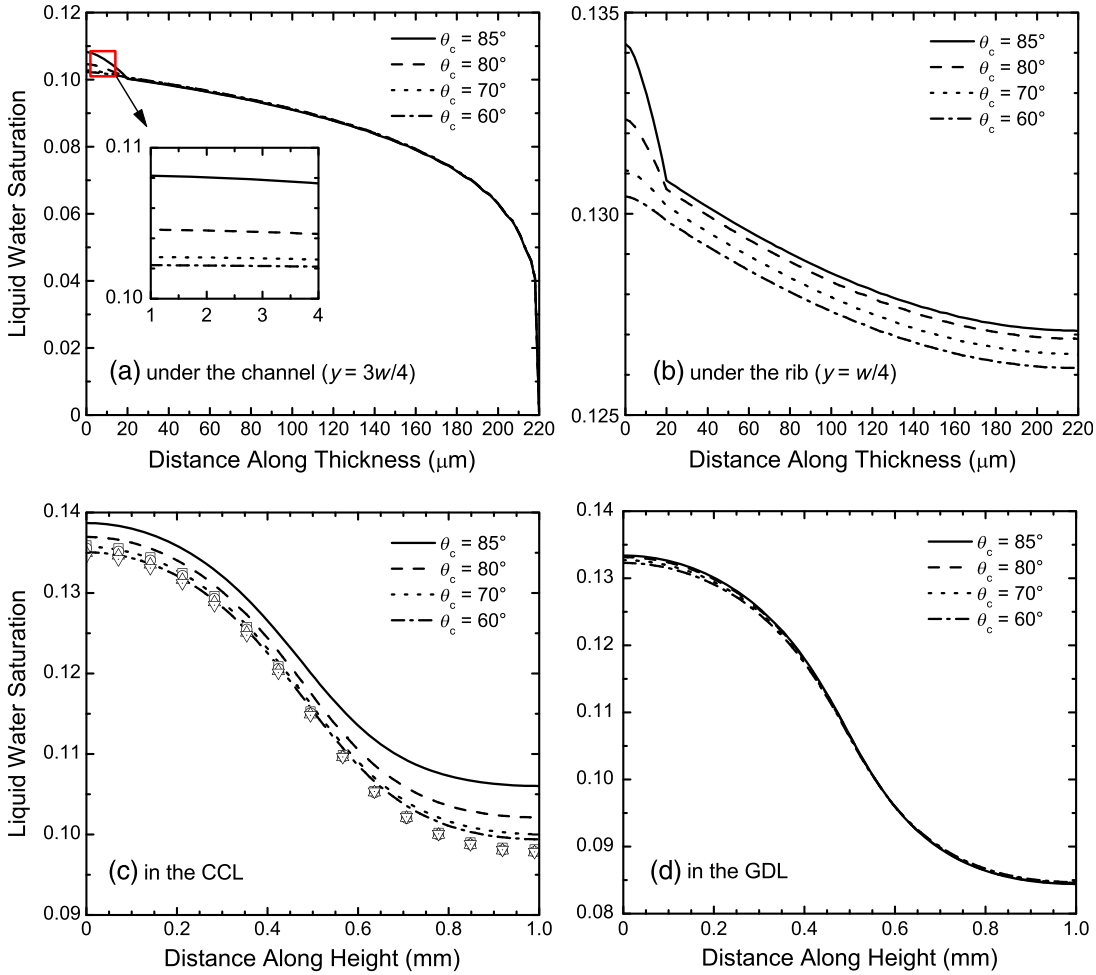

Figure 8. Variations of liquid water saturation with CCL contact angles for a current density of 0.8 A/cm^2, (a) along the through-plane direction of CCL and GDL under the channel, (b) under the rib, (c) in-plane direction of CCL, and (d) in-plane direction of GDL.

saturation inside the CCL under the rib, it seems that the high water saturation in CCL under the rib also slightly influences water saturation inside the GDL under the rib area.

Although the catalyst layer contact angles show a distinct effect on liquid water saturation inside the CCL, the oxygen mass fractions remain unchanged for all these contact angles. The contour plots of oxygen mass fraction inside the CCL and GDL are shown in Figure 9 for two extreme contact angles. As seen in Figure 9 for CCL contact angles, the contours of oxygen mass fraction are exactly the same even inside the catalyst layer. The main reason why we do not observe any significant variation in the oxygen mass fraction is the effective oxygen diffusivity. The amount of variation observed in the liquid saturation profile inside the CCL (Figure 8) is unable to further hinder the oxygen transport or the effective transport properties. It is believed that the reactant transport will only be affected if the pores are completely blocked by liquid water. The effective property formulations available in Ref. [42] were developed based on the assumption that if the pores were partially filled by liquid water, it will only reduce the effective oxygen diffusivity, but the order of magnitude will remain the same. Hence, a significant change will only be observed between the dry case and flooded case. Once a fuel cell is flooded, the oxygen concentration will only be further hindered for extremely high liquid water saturation.

Figure 10 depicts the local activation overpotential profiles along the CCL thickness for different CCL contact angles. Although the liquid water saturation changes about 6% under the flow channel and about 3% under the rib when the CCL contact angle changes from 60° to 85°, the activation overpotentials remain exactly the same for different CCL contact angles. As mentioned in Ref. [43], the linear reduction of active reaction area with liquid water saturation used in the numerical simulation is the main reason for the identical activation overpotential profiles observed in Figure 10. This result also raises the concern whether the linear reduction of active reaction

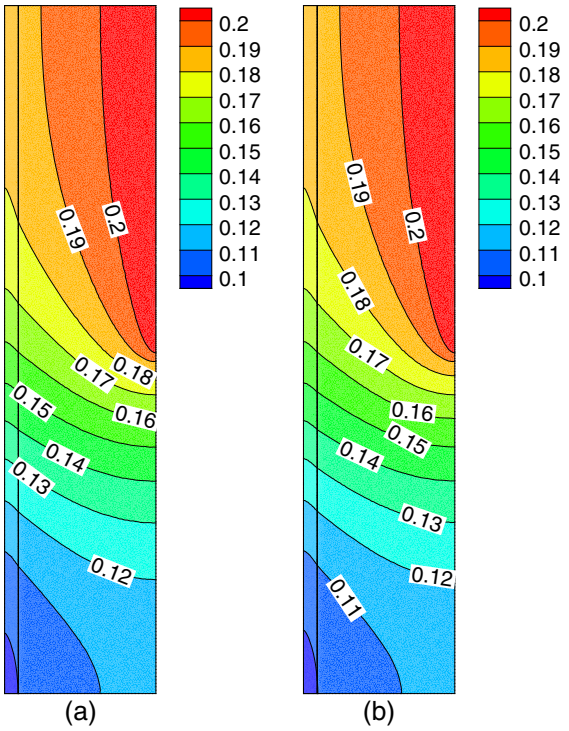

Figure 9. Distributions of oxygen mass fraction inside the cathode catalyst and GDLs for two difference CCL contact angles: (a) $\theta_c = 60^\circ$ and (b) $\theta_c = 85^\circ$.

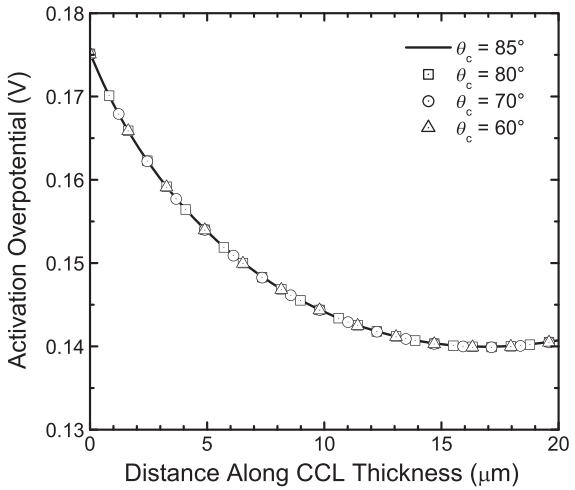

Figure 10. Local activation overpotential profiles along the catalyst layer thickness at $y = w/4$ for different CCL contact angles.

area with liquid water saturation is sufficient for the PEM fuel cell modeling, which has been widely used over the last decades. Although we explored the liquid water transport inside the CCL and how the CCL properties affect the liquid water transport, it seems to be interesting to explore whether the GDL surface wettability or porosity also affects the liquid water transport inside the CCL. In the following sections, the results for several GDL contact angles and porosities are presented.

4.4. Effect of gas diffusion layer contact angle

Figure 11 shows the variations of liquid water saturation and oxygen mass fraction with GDL contact angles at two different locations along the through-plane direction for a current density of 0.8 A/cm^2. The parameter values used in these calculations are listed in Table II, except the GDL contact angles that are indicated in the figure legends.

Int. J. Energy Res. 2011; **35**:1325–1339 © 2011 John Wiley & Sons, Ltd.
DOI: 10.1002/er

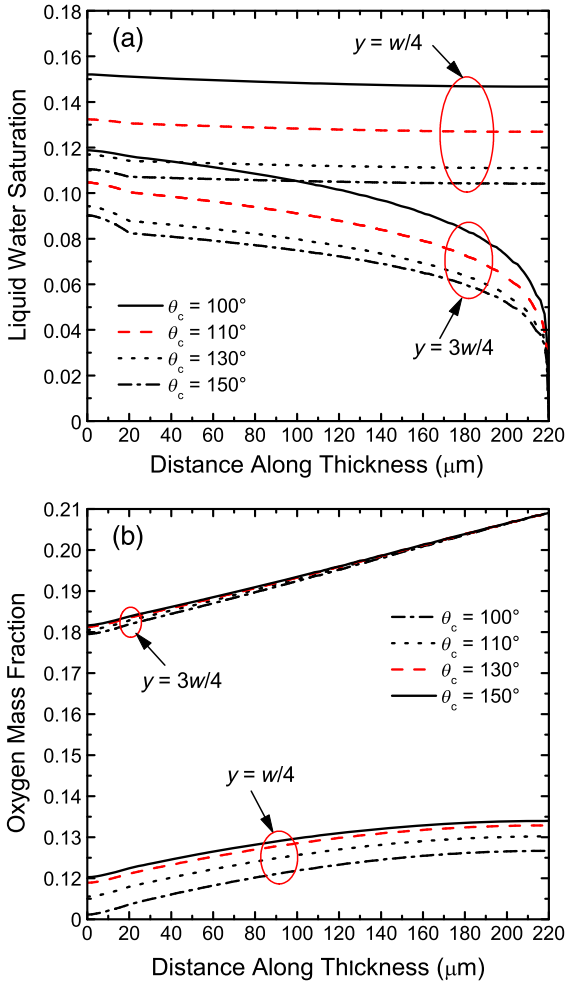

Figure 11. Variations of liquid water saturation and oxygen mass fraction with GDL contact angles along the through-plane direction at $y = 3w/4$ (under the channel) and $y = w/4$ (under the rib).

Unlike the effect of CCL contact angles on the liquid water saturation (Figure 8), the GDL contact angles show a large variation on the liquid water saturation throughout the entire CCL and GDL thicknesses for both locations as shown in Figure 11a. It also indicates that the highest liquid saturation will always be under the rib because of the longer transport path for liquid water to be removed through the GDL to the GFC. It is also clear that the higher the GDL contact angles (hydrophobicity), the lower the liquid water saturations. Hence, the GDL hydrophobicity enhances the liquid water removal from the CCL to the GFC. The phenomenon that the GDL hydrophobicity enhances the liquid water removal from PEM fuel cells has already been reported in various studies [17,19,20], and the present model depicts exactly the similar trend.

The variations of oxygen mass fraction with GDL contact angles inside the CCL and GDL are illustrated in Figure 11b along the through-plane direction at $y = 3w/4$ and $y = w/4$. Although a significant change in liquid saturation is observed with the GDL contact angles, it seems that the amount of liquid saturation observed in Figure 11a does not hinder the oxygen transport, particularly under the flow channel ($y = 3w/4$). However, it does show that the oxygen transport is hindered by the liquid water under the rib. Because the liquid saturation decreases with GDL contact angles, the oxygen mass fraction also decreases with GDL contact angles under the rib ($y = w/4$).

Figure 12 depicts the local activation overpotential profiles in the catalyst layer along the CCL thickness for different GDL contact angles. Similar to the effect of CCL contact angles on the activation overpotentials, the GDL contact angles also show insignificant effect on the activation overpotentials. In fact, the activation overpotentials (highest value at the membrane/CCL interface) for all of the contact angles remain almost constant. The GDL contact angles, however, show local variations that can be attributed to the local variations of oxygen concentration. Although the liquid water saturation reduces about 30% under the rib ($y = w/4$) when the

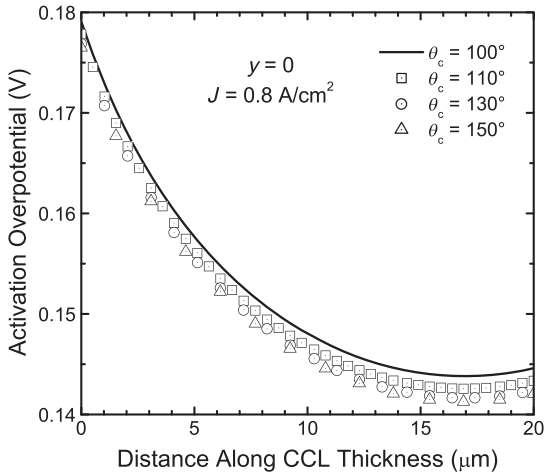

Figure 12. Local activation overpotential profiles along the catalyst layer thickness under the rib at $y = 0$ for different GDL contact angles.

GDL contact angle changes from 100° to 150°, the local activation overpotentials at the membrane/CCL interface, that is, the total activation losses, remain identical. As mentioned earlier that the widely used linear reduction of active reaction area with liquid water saturation is insufficient to capture the effect of liquid saturation on the activation overpotential, Figure 12 is again providing the evidence. Figures 11 and 12 also indicate that the higher GDL contact angles enhance the liquid water removal without significantly hindering the oxygen transport and without increasing the activation losses; hence, a higher GDL contact angle will always improve the fuel cell performance. However, a higher hydrophobicity requires a higher polytetrafluoroethylene (PTFE) loading for the GDL, which may reduce the GDL's electronic and thermal conductivities. Hence, a proper measure should be taken to find the optimum PTFE loading for the GDL. Although the present model is not capable of quantifying the effect of PTFE loading, it indicates new avenues for future research. Overall, the results shown in Figures 11 and 12 provide some useful insights on how GDL hydrophobicity impacts the cell performance and liquid water transport inside the CCL. It is worthwhile to note that the detailed analyses of GDL and microporous layer's properties are available in Ref. [23,44–47].

4.5. Effect of gas diffusion layer porosity

Figure 13 shows the variations of liquid water saturation along the through-plane direction of CCL and GDL for three different values of GDL porosity as indicated in the legend. The liquid saturation profiles are almost uniform throughout the entire thickness under the rib ($y = w/4$), but the liquid saturations decrease with GDL porosities. Hence, liquid transport is hindered by the low GDL porosity. Similar saturation profiles are observed under the flow channel ($y = 3w/4$). Here, liquid water saturation profiles sharply decrease at the GDL/GFC interface, which indicates the removal of liquid water through the flow channel. These results also indicate that the higher GDL porosity will keep the liquid water saturation low inside the CCL.

The local activation overpotential profiles along the CCL thickness with GDL porosities are shown in Figure 14. Because the activation overpotential is seen to be a maximum under the rib, the profiles shown in Figure 14 are plotted along the line of symmetry under the rib. It is observed that changing GDL porosity from 0.7 to 0.6 yields about 7.4% reduction of activation loss, whereas the reduction of activation loss is about 2.7% when GDL porosity changes from 0.6 to 0.5. Hence, a GDL porosity of 0.6 would provide a better cell performance without sacrificing the significant amount of cell output. Clearly,

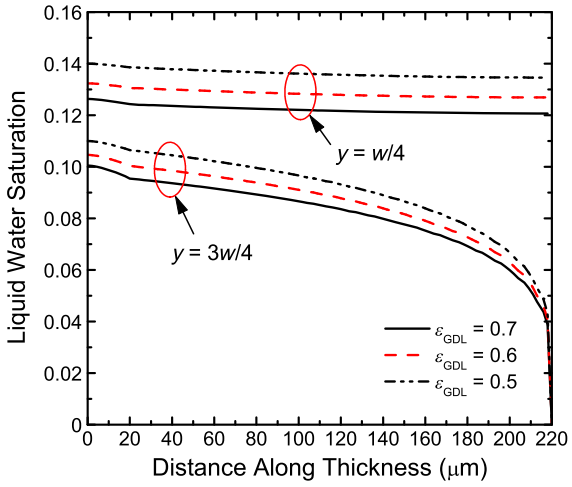

Figure 13. Variations of liquid water saturation with GDL porosity along the through-plane direction at $y = 3w/4$ (under the channel) and $y = w/4$ (under the rib).

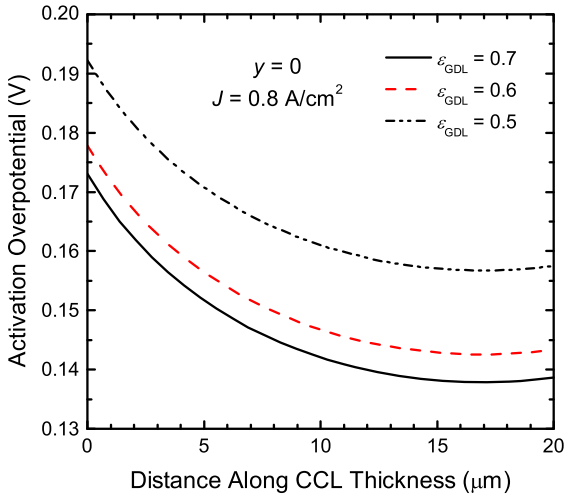

Figure 14. Local activation overpotential profile along the catalyst layer thickness under the rib at $y = 0$ for different GDL porosities.

the results shown in Figures 13 and 14 suggest that the higher GDL porosity is always favorable for the liquid water transport, which will eventually provide better reactant transport, and it would also be possible to run the fuel cell at a higher current density without the concentration polarization losses. At the same time, we should keep it in mind that the higher GDL porosity would reduce the mechanical strength of GDL.

5. CONCLUSIONS

A two-phase numerical model of liquid water transport in the CCL of a PEM fuel cell has been developed to investigate the effects of catalyst layer structure and wettability on transport processes and fuel cell performance. The governing conservation equations have been derived from the microscopic conservation equations using a volume-averaged technique. The numerical results have been compared with literature, and a good agreement has been observed. It has also been observed that the catalyst layer wetting properties control the flooding behavior inside the CCL, and the mobile liquid water saturation in a hydrophilic CCL can be reduced by increasing the surface wettability or lowering the contact angle. However, the catalyst layer wettability has little influence on the liquid water transport inside the GDL. A similar statement can be made for the oxygen transport through the GDL. Conversely, the CCL structure (platinum and Nafion loadings) has a significant effect on both the liquid water and oxygen transports throughout the CCL and GDL thicknesses. Furthermore, the linear reduction of active reaction area with liquid water saturation seems insufficient to capture the true nature of oxygen transport because the linear reduction approach overestimates the active reaction surface area inside the CCL. The catalyst layer surface wettability has not shown any significant effect on the activation overpotential, hence neither on the cell performance. However, surface wettability may reduce the cell performance depending on the true relationship between the active reaction surface area and liquid water flooding. Overall, the results of this study provide insight on how the CCL structure and wettability can be optimized to improve the fuel cell performance and reduce water flooding inside the CCL.

NOMENCLATURE

A	interfacial mass-transfer rate, kg/m^3 Pa s
A_s	catalyst surface area per unit mass of catalyst, m^2/kg
A_v	reactive surface area per unit volume, 1/m
c	concentration, mol/m^3
F	Faraday's constant, C/mol
J	current density, A/cm^2
k_r	relative permeability
K	permeability, m^2
M	molecular weight, kg/mol
P	pressure, Pa
P_c	capillary pressure, Pa
P_{sat}	saturation pressure, Pa
R	gas constant, J/mol K
s	saturation
T	temperature, K
u	velocity, m/s
w	mass fraction
x	mole fraction
γ	surface tension, N/m
α_a, α_c	anodic and cathodic transfer coefficients, respectively
Γ	source term
δ	thickness, m
ε	porosity, volume fraction
η_c	activation overpotential, V

μ	viscosity, Pa s
Ω	computational boundary
Φ	potential, V
ρ	density, kg/m^3
θ_c	contact angle, °
σ	conductivity, S/m

CL	catalyst layer
eff	effective value
g	gas phase
l	liquid phase
m	membrane phase
Pt	platinum
O_2	oxygen
ref	reference value
H_2O	water

BP	bipolar plate
CCL	cathode catalyst layer
GDL	gas diffusion layer
GFC	gas flow channel
PEM	polymer electrolyte membrane

ACKNOWLEDGEMENT

The financial support of the Natural Sciences and Engineering Research Council of Canada is gratefully acknowledged.

REFERENCES

1. Weber AZ, Newman J. Modeling transport in polymer-electrolyte fuel cells. *Chemical Reviews* 2004; **104**:4679–4726.
2. Wang CY. Fundamental models for fuel cell engineering. *Chemical Reviews* 2004; **104**:4727–4765.
3. Dincer I. Environmental and sustainability aspects of hydrogen and fuel cell systems. *International Journal of Energy Research* 2007; **31**:29–55.
4. Barbir F, Yazici S. Status and development of PEM fuel cell technology. *International Journal of Energy Research* 2008; **32**:369–378.
5. Meng H. Numerical investigation of transient responses of a PEM fuel cell using a two-phase non-isothermal mixed-domain model. *Journal of Power Sources* 2007; **171**:738–746.
6. Nam J, Lee K, Hwang G, Kim C, Kaviany M. Microporous layer for water morphology control in PEMFC. *International Journal of Heat and Mass Transfer* 2009; **52**:2779–2791.
7. Meng H. Multi-dimensional liquid water transport in the cathode of a PEM fuel cell with consideration of the micro-porous layer. *International Journal of Hydrogen Energy* 2009; **34**:5488–5497.
8. Jung C, Park C, Lee Y, Kim W, Yi S. Numerical analysis of catalyst agglomerates and liquid water transport in proton exchange membrane fuel cells. *International Journal of Hydrogen Energy* 2010; **35**:8433–8445.
9. Springer TE, Zawodzinski TA, Gottesfeld S. Polymer electrolyte fuel cell model. *Journal of the Electrochemical Society* 1991; **138**:2334–2342.
10. Bernardi DM, Verbrugge MW. Mathematical model of a gas diffusion electrode bonded to a polymer electrolyte. *AIChE Journal* 1991; **37**:1151–1163.
11. Fuller TF, Newman J. Water and thermal management in solid-polymer-electrolyte fuel cells. *Journal of the Electrochemical Society* 1993; **140**:1218–1225.
12. Yamada H, Hatanaka T, Murata H, Morimoto Y. Measurement of flooding in gas diffusion layers of polymer electrolyte fuel cells with conventional flow field. *Journal of the Electrochemical Society* 2006; **153**:A1748–A1754.
13. Jung UH, Jeong SU, Park KT, Lee HM, Chun K, Choi DW, Kim SH. Improvement of water management in air-breathing and air-blowing PEMFC at low temperature using hydrophilic silica nano-particles. *International Journal of Hydrogen Energy* 2007; **32**:4459–4465.
14. Liu X, Guo H, Ye F, Ma CF. Flow dynamic characteristics in flow field of proton exchange membrane fuel cells. *International Journal of Hydrogen Energy* 2008; **33**:1040–1051.
15. Owejan JP, Gagliardo JJ, Sergi JM, Kandlikar SG, Trabold TA. Water management studies in PEM fuel cells, Part I: Fuel cell design and in-situ water distributions. *International Journal of Hydrogen Energy* 2009; **34**:3436–3444.
16. Lu Z, Kandlikar SG, Rath C, Grimm M, Domigan W, White AD, Hardbarger M, Owejan JP, Trabold TA. Water management studies in PEM fuel cells, Part II: Ex-situ investigation of flow maldistribution, pressure drop and two-phase flow pattern in gas channels. *International Journal of Hydrogen Energy* 2009; **34**:3445–3456.
17. Nam JH, Kaviany M. Effective diffusivity and water-saturation distribution in single- and two-layer PEMFC diffusion medium. *International Journal of Heat and Mass Transfer* 2003; **46**:4595–4611.
18. Natarajan D, Nguyen TV. Three-dimensional effect of liquid water flooding in the cathode of a PEM fuel cell. *Journal of Power Sources* 2003; **115**:66–80.
19. Weber AZ, Darling RM, Newman J. Modeling two-phase behavior in PEFCs. *Journal of the Electrochemical Society* 2004; **151**:A1715–A1727.
20. Pasaogullari U, Wang CY. Liquid water transport in gas diffusion layer of polymer electrolyte fuel cells. *Journal of the Electrochemical Society* 2004; **151**: A399–A406.

21. Chen KS, Hickner MA, Noble DR. Simplified models for predicting the onset of liquid water droplet instability at the gas diffusion layer/gas flow channel interface. *International Journal of Energy Research* 2005; **29**:1113–1132.
22. Pasaogullari U, Wang CY. Two-phase modeling and flooding prediction of polymer electrolyte fuel cells. *Journal of the Electrochemical Society* 2005; **152**: A380–A390.
23. Weber AZ, Newman J. Effects of microporous layers in polymer electrolyte fuel cells. *Journal of the Electrochemical Society* 2005; **152**:A677–A688.
24. Song DT, Wang QP, Liu ZS, Huang C. Transient analysis for the cathode gas diffusion layer of PEM fuel cells. *Journal of Power Sources* 2006; **159**:928–942.
25. Spernjak D, Prasad A, Advani S. Experimental investigation of liquid water formation and transport in a transparent single-serpentine PEM fuel cell. *Journal of Power Sources* 2007; **170**:334–344.
26. Ren G, Yu L, Qin M, Jiang X. Transport mechanisms and performance simulation of a PEM fuel cell. *International Journal of Energy Research* 2008; **32**:514–530.
27. Park YH, Caton JA. Monitoring an electrode flooding through the back pressure in a proton exchange membrane fuel cell. *International Journal of Green Energy* 2008; **5**:347–359.
28. Basu S, Li J, Wang CY. Two-phase flow and maldistribution in gas channels of a polymer electrolyte fuel cell. *Journal of Power Sources* 2009; **187**:431–443.
29. Wu H, Li X, Berg P. On the modeling of water transport in polymer electrolyte membrane fuel cells. *Electrochimica Acta* 2009; **54**:6913–6927.
30. Zhang J, Li H, Shi Z, Zhang J. Effects of hardware design and operation conditions on PEM fuel cell water flooding. *International Journal of Green Energy* 2010; **7**:461–474.
31. Das PK, Li X, Liu ZS. A three-dimensional agglomerate model for the cathode catalyst layer in PEM fuel cells. *Journal of Power Sources* 2008; **179**:186–199.
32. Das PK, Li X, Liu ZS. Analytical approach to polymer electrolyte membrane fuel cell performance and optimization. *Journal of Electroanalytical Chemistry* 2007; **604**:72–90.
33. Feindel KW, LaRocque LPA, Starke D, Bergens SH, Wasylishen RE. In-situ observations of water production and distribution in an operating H_2/O_2 PEM fuel cell assembly using 1H NMR microscopy. *Journal of the American Chemical Society* 2004; **126**:11436–11437.
34. Bellows RJ, Lin MY, Arif M, Thompson AK, Jacobson DJ. Neutron imaging technique for in-situ measurement of water transport gradients within Nafion in polymer electrolyte fuel cells. *Journal of the Electrochemical Society* 1999; **146**:1099–1103.
35. Baschuk JJ, Li X. A general formulation for a mathematical PEM fuel cell model. *Journal of Power Sources* 2004; **142**:134–153.
36. Gurau V, Edwards RV, Mann JA, Zawodzinski TA. A look at the multi-phase mixture model for PEM fuel cell simulations. *Electrochemical and Solid-State Letters* 2008; **11**:B132–B135.
37. Das PK. Transport phenomena in cathode catalyst layer of PEM fuel cells. Ph.D. thesis, University of Waterloo, June 2010. Available from: http://hdl.handle.net/10012/5282
38. Whitaker S. Diffusion and dispersion in porous media. *AIChE Journal* 1967; **13**:420–427.
39. Whitaker S. The transport equations for multi-phase systems. *Chemical Engineering Science* 1971; **28**:139–147.
40. Gray WG. A derivation of the equations for multiphase transport. *Chemical Engineering Science* 1975; **30**:229–233.
41. Leverett M. Capillary behavior in porous solids. *Transactions of AIME* 1941; **142**:152–169.
42. Das PK, Li X, Liu ZS. Effective transport coefficients in PEM fuel cell catalyst and gas diffusion layers: beyond Bruggeman approximation. *Applied Energy* 2010; **87**:2785–2796.
43. Das PK, Li X, Liu ZS. Analysis of liquid water transport in cathode catalyst layer of PEM fuel cells. *International Journal of Hydrogen Energy* 2010; **35**:2403–2416.
44. Kong CS, Kim DY, Lee HK, Shul YG, Lee TH. Influence of pore-size distribution of diffusion layer on mass-transport problems of proton exchange membrane fuel cells. *Journal of Power Sources* 2002, **108**:185–191.
45. Qi Z, Kaufman A. Improvement of water management by a microporous sublayer for PEM fuel cells. *Journal of Power Sources* 2002; **109**:38–46.
46. Zhang ZQ, Jia L. Parametric study of the porous cathode in the PEM fuel cell. *International Journal of Energy Research* 2009; **33**:52–61.
47. Weber AZ. Improved modeling and understanding of diffusion-media wettability on polymer-electrolyte-fuel-cell performance. *Journal of Power Sources* 2010; **195**:5292–5304.